Proceedings of FUELCELL2006
The 4th International Conference on FUEL CELL SCIENCE, ENGINEERING and TECHNOLOGY
June 19-21, 2006, Irvine, CA

FUELCELL2006-97112

NUMERICAL ANALYSIS OF HEAT/MASS TRANSFER AND ELECTROCHEMICAL REACTION IN AN ANODE-SUPPORTED FLAT-TUBE SOLID OXIDE FUEL CELL

Masayuki Suzuki, Naoki Shikazono, Koji Fukagata, Nobuhide Kasagi

The University of Tokyo
Department of Mechanical Engineering
Hongo 7-3-1, Bunkyo-ku, Tokyo, 113-8656, Japan

ABSTRACT

Three-dimensional heat and mass transfer and electrochemical reaction in an anode-supported flat-tube solid oxide fuel cell (FT-SOFC) are studied. Transport and reaction phenomena mainly change in the streamwise direction. Exceptionally, hydrogen and water vapor have large concentration gradients also in the cross section perpendicular to the flow direction, because of the insufficient mass diffusion in the porous anode. Based on these results, we develop a simplified one-dimensional cell model. The distributions of temperature, current, and overpotential predicted by this model show good agreement with those obtained by the full three-dimensional simulation. We also investigate the effects of pore size, porosity and configuration of the anode on the cell performance. Extensive parametric studies reveal that, for a fixed three-phase boundary (TPB) length, rough material grains are preferable to obtain higher output voltage. In addition, when the cell has a thin anode with narrow ribs, drastic increase in the volumetric power density can be achieved with small voltage drop.

Keywords: Solid oxide fuel cell, Simulation, Heat and mass transfer, Electrochemical reaction, Modeling

1. INTRODUCTION

Investigation of detailed heat/mass transfer and electrochemical reaction characteristics in the cell is essential for further improving performance of solid oxide fuel cell (SOFC). For such purpose, a series of numerical simulation is expected to be useful.

To date, a number of numerical simulation studies have been reported for various types of SOFCs. Ferguson et al. (1996) carried out simulation for planar, tubular, and cylindrical cells with simplified one-dimensional cell models. They found that the anode and interconnector sizes have considerable impact on the planar cell performance. Chan et al. (2001) investigated the performance of planar SOFCs with a simplified cell model. They focused on the thicknesses of electrolyte and electrodes, and pointed out possible advantages of anode-supported cell configuration. Aguir et al. (2004) also numerically assessed the influence of various operating conditions on the anode-supported cell performance. With this kind of simplified simulation, we can predict cell performance at a reasonable computational cost. On the other hand, further detailed simulation is also required to validate these simplified cell models.

Several studies have more intensively focused on the flow and reaction fields in the cell with three-dimensional simulations. Li and Chyu (2005) analyzed the characteristics of heat and mass transfer in a tubular SOFC. Yakabe et al. (2000) showed the distributions of flow and reaction fields, and thermal stress in a planar SOFC for different flow arrangements.

Recently, a flat-tube SOFC (FT-SOFC) has attracted much attention among various cell configurations due to its high power density and relative easiness of fabrication and gas sealing (Giuseppe, 2005). In the present study, we perform numerical simulation of heat and mass transfer and electrochemical reaction in an anode-supported FT-SOFC. The final goal is to obtain clues for designing a cell of higher performance. For this purpose, we first discuss the characteristics of flow and reaction fields in the cell through three-dimensional simulation. Subsequently, we propose a simplified one-dimensional plug-flow cell model. Then, we assess the effects of design parameters on the cell performance by using this simplified cell model. A special attention is paid on the geometrical configuration and microstructure of the porous anode.

2. SIMULATION MODEL AND GOVERNING EQUATIONS

2.1 COMPUTATIONAL MODEL

The anode-supported FT-SOFC is assumed to have a periodic structure in the spanwise (z-) direction. The air and fuel flows are symmetric in each flow passage since their Reynolds numbers are low (1–50). Thus, as shown in Fig. 1, only half of

Copyright © 2006 by ASME

Table 1 Physical properties of cell components.

Component	ρ [10^3kg/m^3] [a]	C_p [kJ/kg K] [a]	λ [W/mK] [a]	σ [Ω cm]	ε [-]	τ [-]	d_p [μm]
Electrolyte	5.48	0.45	2.0	$3.0\times10^{-3}\exp(10300/T)$ [b]	-	-	-
Cathode	5.62	0.45	11.0	$8.11\times10^{-3}\exp(600/T)$ [c]	0.5	3.0	1.0
Anode	6.5	0.45	10.0	$2.98\times10^{-3}\exp(-1392/T)$ [b]	0.4–0.6	Eq. (1)	0.2–2.0
Interconnector	6.5	0.55	6.0	2.5 [a]	-	-	-

a: National institute of Advanced Industrial Science and Technology (AIST) Web Site (http://unit.aist.go.jp/energy/fuelcells/database/index.html ; Japanese)
b: Campanari and Iora (2004) c: Aguiar et al. (2004)

the periodic structure is taken as a computational domain. The unit cell is composed of an electrolyte layer, a cathode, an anode with fuel channel, an interconnector, and an air passage between the adjacent cells. The anode has also a role as a mechanical support of the cell. The air and fuel are in co-flow arrangement. The physical properties of each cell component listed in Table 1 are assumed to be constant except for the resistivity, which is dependent on temperature. The tortuosity of the porous electrodes correlates with the porosity (Carniglia, 1986). In the present study, the tortuosity of the anode τ_{an} is simply treated as a function of the porosity:

$$\tau_{an} = 5.0 - 4\varepsilon_{an} \qquad (1)$$

The interface between the electrolyte and electrodes are treated as the three-phase boundary (TPB). The electrodes are porous, while the electrolyte and interconnector are treated as solid. The anode rib width $l_{z,rib}$, thickness $l_{y,an}$, porosity ε_{an} and pore diameter $d_{p,an}$ are varied as simulation parameters. In the reference case, the cell has dimensions of $l_{z,rib}$, = 1.5 mm and $l_{y,an}$ = 1.0 mm, with ε_{an} and $d_{p,an}$ being selected as 0.5 and 1.0 μm, respectively.

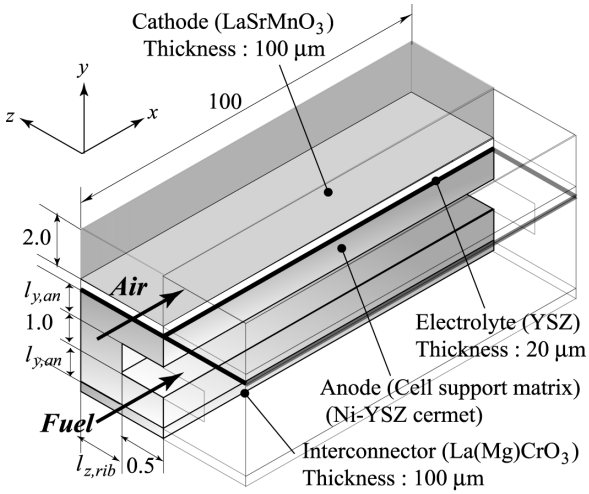

Fig. 1 Computational model of the cell.

Table 2 Operating conditions of the cell.

Inlet gas temperature and pressure	600 °C, 1.0 atm
Electrolyte average current density	0.25, 0.5, 0.75 A/cm^2
Utilization rate of O_2 and H_2	0.3, 0.85

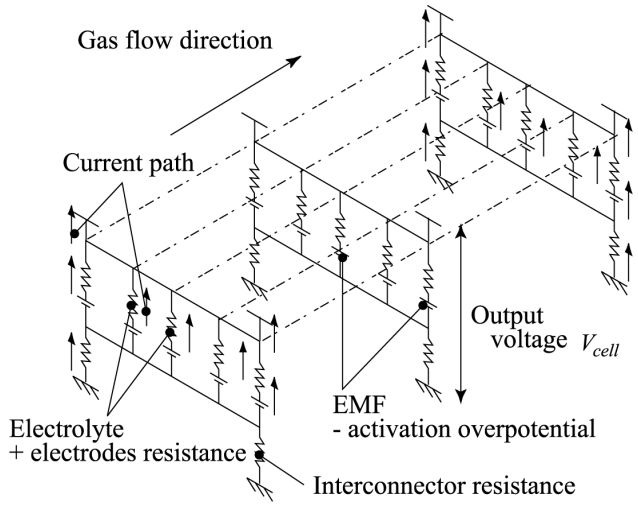

Fig. 2 Equivalent electrical circuit of the cell.

The electrochemical reaction is calculated using an equivalent circuit shown in Fig. 2. This model consists of the electromotive force (EMF) generated in the cell, the current density, and the componential losses of the cell, *i.e.*, the ohmic loss and the activation and concentration overpotentials. The cathode and the interconnector surface are treated as equi-potential, and the average current density of the electrolyte is kept constant (see Table 2). Since the steady-state performance of the cell is discussed in the present study, the capacitance between electrolyte and electrodes is neglected.

Other operating conditions are listed in Table 2. The completely reformed methane (with steam to carbon ratio = 2.5) is selected as a fuel inlet composition (H_2 : H_2O : CO_2 = 8 : 1 : 2). The solid and porous boundaries at the cell inlet and outlet are treated as adiabatic. The thermal boundary conditions at the upper and lower boundary of the computational domain are periodic in the perpendicular (*y*-) direction.

2.2 GOVERNING EQUATIONS

The governing equations for the reactive fluids are the mass conservation, Navier-Stokes, energy and chemical species transport equations:

Copyright © 2006 by ASME

$$\frac{\partial(\varepsilon\rho)}{\partial t}+\nabla\cdot(\varepsilon\rho\mathbf{u})=0, \tag{2}$$

$$\frac{\partial(\varepsilon\rho\mathbf{u})}{\partial t}+\nabla\cdot\{(\varepsilon\rho\mathbf{u})\mathbf{u}\} = -\nabla(\varepsilon P)+\nabla\cdot\left[\varepsilon\mu\left(\nabla\cdot u+\frac{\partial u_j}{\partial x_i}-\frac{2}{3}\delta_{ij}\frac{\partial u_k}{\partial x_k}\right)\right]-\frac{\varepsilon^2\mu}{\kappa}u, \tag{3}$$

$$\frac{\partial\left[\{\varepsilon\rho_{gas}C_{p,gas}+(1-\varepsilon)\rho_{sol}C_{p,sol}\}T\right]}{\partial t}+\nabla\cdot\left(\varepsilon\rho_{gas}C_{p,gas}\mathbf{u}T\right) = \nabla\cdot\left[\{\varepsilon\lambda_{p,gas}+(1-\varepsilon)\lambda_{p,sol}\}\nabla T\right]+Q, \tag{4}$$

$$\frac{\partial(\varepsilon\rho Y_i)}{\partial t}+\nabla\cdot(\varepsilon\rho\mathbf{u}Y_i)=\nabla\cdot(\varepsilon\rho D_{i,eff}\nabla Y_i). \tag{5}$$

Note that, by definition, the summation of Eq. (5) for all reactants is identical to Eq. (1). The Darcy's law is introduced to describe the friction resistance in the porous media (the last term in Eq. (3)). The physical properties of the fluid are treated as functions of the local temperature and concentration of reactants (Bird et al., 2002). The effective diffusivity of reactant *i* in the porous media ($D_{i,eff}$ in Eq. (5)) is calculated by the parallel pore model (Asaeda et al., 1974), which reads

$$D_{i,eff}=\frac{\varepsilon}{\tau}\left(\frac{1-Y_i\left(1-\sqrt{M_i/M_{mix}}\right)}{D_{im}}+\frac{1}{D_{ik}}\right)^{-1}, \tag{6}$$

where D_{im} and D_{ik} are the multicomponent molecular diffusivity and the Knudsen diffusivity of reactant *i*, respectively, and M_{mix} represents the averaged molar weight of the fluid.

The second-order accurate central finite difference method with Euler explicit scheme is employed for discretization of each equation, and the flow continuity is ensured by the SMAC method. The number of computational grids is $64\times21\times16$ (*x* by *y* by *z*) for the air-side and $64\times15\times16$ for the fuel-side. The low-Mach number approximation (Majda and Sethian, 1985) is introduced for efficient computation of the heat and mass transfer considering variable physical properties.

The local current density *i* and the ohmic losses η_{ohm} of cell components are computed by using the Ohm's and Kirchhoff's laws with resistivities σ shown in Table 1. The EMF is computed by the Nernst equation,

$$E=-\frac{\Delta G^o_{H_2O}}{2F}+\frac{RT}{4F}\ln\left\{\frac{p^2_{H_2}p_{O_2}}{p^2_{H_2O}}\right\}. \tag{7}$$

Table 3 Parameters for activation overpotential.

Parameter	Cathode	Anode
Activation energy E_{act} [kJ/mol]	140	120
Pre-exponential factor γ[A/m^2]	5.0×10^9	5.0×10^9

The concentration overpotential is defined as the difference between the EMF derived from the mean concentration of reactants in each corss section E_{bulk} and the local value on the TPB E_{TPB},

$$\eta_{con}=E_{bulk}-E_{TPB}=\frac{RT}{2F}\ln\left\{\frac{\left(\bar{p}_{O_2}/p_{O_2,TPB}\right)^{1/2}\left(\bar{p}_{H_2}/p_{H_2,TPB}\right)}{\left(\bar{p}_{H_2O}/p_{H_2O,TPB}\right)}\right\}. \tag{8}$$

The activation overpotentials in the cathode and anode are calculated by using the Butler-Volmer equation,

$$i_{ele}=i_o\left\{exp\left(\frac{\alpha nF\eta_{act}}{RT}\right)-exp\left(-\frac{(1-\alpha)nF\eta_{act}}{RT}\right)\right\}, \tag{9}$$

where α and *n* are the transfer coefficient ($0<\alpha<1$) and the number of electrons participating in the reaction, respectively. In the present study, α=0.5, and *n* = 4 (for cathode) or 2 (for anode) are assumed. The exchange current densities i_o are written as follows (Costamagna & Honegger, 1998) :

$$i_{o,ca}=\gamma_{ca}\left(\frac{p_{O_2,TPB}}{P}\right)^{1/4}\exp\left(\frac{-E_{act,ca}}{RT}\right), \qquad i_{o,an}=\gamma_{an}\left(\frac{p_{H_2,TPB}}{P}\right)\left(\frac{p_{H_2O,TPB}}{P}\right)^{-1/2}\exp\left(\frac{-E_{act,an}}{RT}\right), \tag{10}$$

where γ and E_{act} are pre-exponential factor and the activation energy of the electrode, respectively. Following previous researches of Campanari and Iora (2004), Aguiar et al. (2004), and Costamagna and Honegger (2000), the values of these parameters are chosen as shown in Table 3. The output voltage of the cell V_{cell} is

$$V_{cell}=E-(\eta_{ohm}+\eta_{act}+\eta_{con}). \tag{11}$$

The local heat production in Eq. (4) is determined by the distributions of overpotentials and local amount of reaction.

3. CHARACTERISTICS OF TRANSPORT AND REACTION PHENOMENA

3.1 HEAT AND MASS TRANSFER

Figure 3 illustrates the lateral distribution of the electrolyte temperature and those of concentrations (molar fraction) of O_2, H_2 and H_2O on the TPB. The heat generated by the exothermic reaction is convected by air and fuel. As a result, the temperature increases monotonously from the cell inlet toward the outlet. Each reactant has also a large concentration gradient in the streamwise (*x*-) direction. These profiles are characterized by the rates of consumption and production of each chemical species during the reaction.

Figure 4 shows the normalized velocity vectors and molar fractions of H_2 and H_2O in the *y*-*z* plane. Large variations of H_2

Copyright © 2006 by ASME

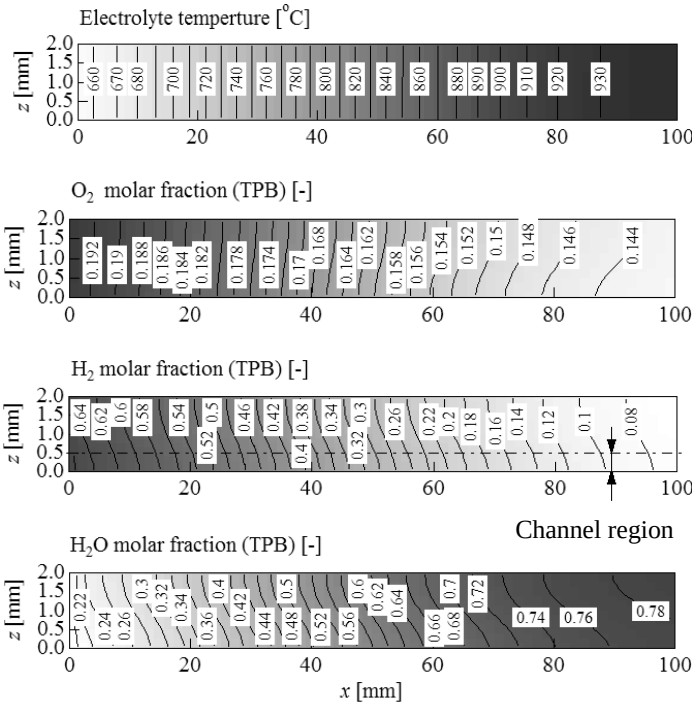

Fig. 3 Lateral distributions of electrolyte temperature and molar fraction of O_2, H_2, H_2O on the TPB.

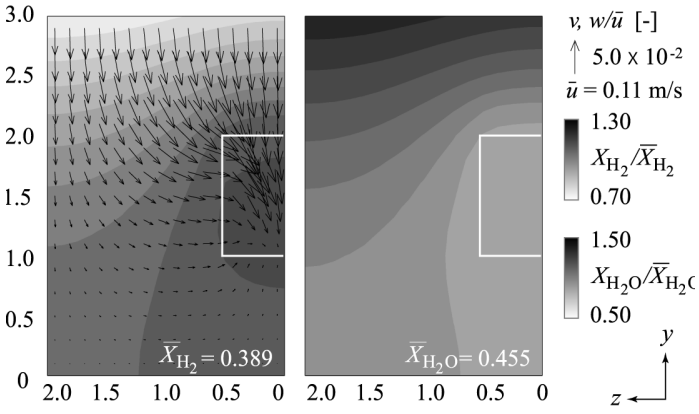

Fig. 4 Cross sectional distributions of normalized velocity vectors (v, w) and molar fractions of H_2 and H_2O at x = 50.

and H_2O are observed in this thick anode. A secondary flow is generated by the migration of O_2 ions from cathode to anode. However, its intensity is negligibly small compared to the main stream of fuel. In fact, the time scale of convection is much shorter than that of mass diffusion or heat conduction. Thus, the convection has negligible impact on the heat and reactant transport in the cross section.

The magnitude of reactant diffusion inside the porous media becomes about ten times smaller than that in the main flow region. This is due to the reduced effective diffusivity in the porous media. For some geometrical configurations, this

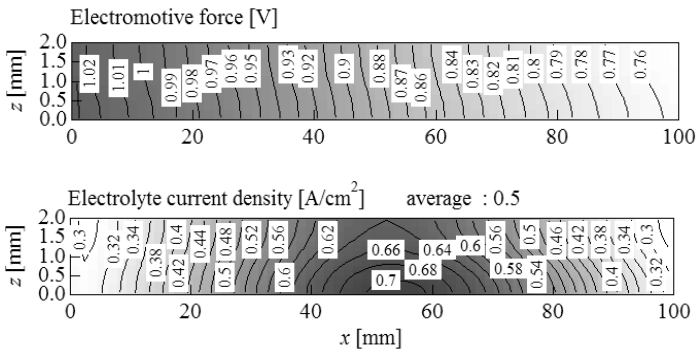

Fig. 5 Distributions of electromotive force (EMF) and electrolyte current density.

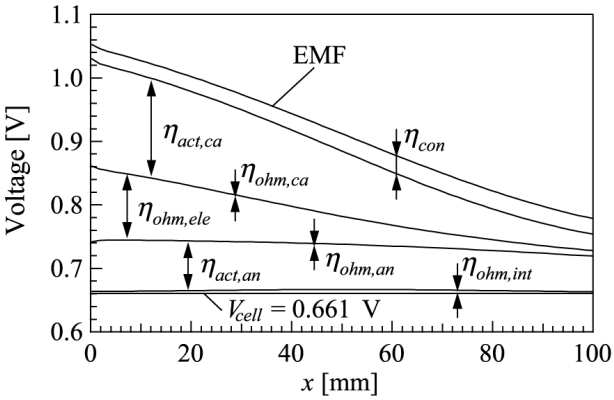

Fig. 6 Distributions of EMF and overpotentials in the cell . (Reference case, averaged in the spanwise direction)

insufficient diffusion of reactants results in the shortage of H_2 and stagnation of H_2O on the TPB.

In contrast, the concentration gradient of O_2 in the thin cathode is considerably small. The solid temperature also shows small gradient in each cross section. This is attributed to the considerably small Biot number (less than 0.1 based on the anode thickness).

3.2 ELECTROCHEMICAL REACTION

Figure 5 shows the distributions of EMF and current density in the electrolyte i_{ele}. The former shows a large gradient in the streamwise direction and a small gradient in spanwise direction. The EMF is maximized at the cell inlet and gradually decreases toward the cell outlet as O_2 and H_2 are consumed and H_2O is produced. In contrast, the maximum of i_{ele} appears in the middle of the cell, because i_{ele} is determined by the local balance between the EMF and the overpotentials.

Figure 6 shows the distributions of componential losses along the streamwise direction. It reveals that dominant components of the voltage loss are the activation overpotential (η_{act}), the concentration overpotential (η_{con}), and the ohmic loss of the electrolyte ($\eta_{ohm,\,ele}$). The cathodic activation overpotential $\eta_{act,ca}$ and $\eta_{ohm,\,ele}$ are maximized at the cell inlet. This is natural

Copyright © 2006 by ASME

because these losses strongly depend on the temperature and become larger as the temperature drops. The anodic activation overpotential ($\eta_{act,an}$) depends on i_{ele}, the local concentrations and the temperature. As a result, $\eta_{act,an}$ is almost constant over the streamwise cell length. The ohmic losses of electrodes ($\eta_{ohm,ca}$ and $\eta_{ohm,an}$) and interconnector ($\eta_{ohm,int}$) are negligibly small because of their small resistivities.

4. PARAMETRIC SURVEY OF ANODE DESIGN

4.1. DEVELOPMENT OF SIMPLIFED CELL MODEL

As shown in the previous section, detailed physical phenomena in the cell can be studied by three-dimensional simulation. However, this simulation requires a large amount of computational load. The present study confirms that the convection and reaction distribution in the perpendicular and lateral directions can be neglected. Therefore, we develop a simplified one-dimensional plug-flow model of the cell as follows.

In the simplified model, the solid components of the cell are separated into six segments as shown in Fig. 7(a). The effect of the anode design is investigated by changing the microstructure and size of elements 3, 4 and 5. The representative temperature is defined in each segment.

The distributions of flow and reaction fields are considered only in the streamwise (x-) direction. However, as shown in Fig. 4, distributions of H_2 and H_2O in the cross section cannot be neglected. Therefore, the following procedures are used to obtain the average concentration of H_2 and H_2O on the TPB.

The boundary condition of reactant i on the TPB for full three-dimensional simulation is

$$\left.\frac{\partial(\varepsilon\rho Y_i)}{\partial y}\right|_{TPB} = \frac{\dot{m}_i}{D_{i,eff}} = \pm\frac{i_{ele}M_i}{2FD_{i,eff}} . \qquad (12)$$

In Eq. (12), $\dot{m}_i$ (kg/m^{2}s) corresponds to the mass consumption of H_2 and the production of H_2O. Thus, the sign of the last term of Eq. (12) is plus for H_2 and minus for H_2O. The mass fraction Y_i can be expressed by using the molar fraction X_i and the molar weight M_i,

$$Y_i = \frac{X_i M_i}{\sum_j (X_j M_j)} . \qquad (13)$$

As shown in Fig. 4, the variations of H_2 and H_2O molar (mass) fractions in the fuel channel are negligibly small and can be assumed as uniform. With this assumption, the normalized mass fraction of reactant f is defined as

$$\phi(y,z) = \frac{Y_i(y,z) - Y_{i,TPB}}{Y_{i,ch} - Y_{i,TPB}}, \qquad (14)$$

where $Y_{i,ch}$ and $Y_{i,TPB}$ are the representative mass fractions of reactant i in the fuel channel and on the TPB, respectively. Namely, ϕ is set as 1 in the channel and 0 on the TPB. The spanwise gradient of ϕ is 0 on the symmetric plane that exists on both sides of the unit cell. The space derivative of ϕ in the perpendicular (y-) direction is written as

$$\frac{\partial\phi}{\partial y} = \frac{1}{Y_{i,ch} - Y_{i,TPB}} \cdot \frac{\partial Y_i}{\partial y} . \qquad (15)$$

Then, the molar fraction of reactant i on the TPB is expressed as a combination of Eqs. (12), (13), (15) and the gas state equation involving an assumption that the physical properties are constant:

$$X_{i,TPB} = X_{i,ch} \pm \frac{i_{ele}}{2F}\frac{RT}{PD_{i,eff}}\frac{1}{\left.\frac{\partial\phi}{\partial y}\right|_{TPB}} . \qquad (16)$$

The gradient of ϕ on the TPB $\left.(\partial\phi/\partial y)\right|_{TPB}$ only depends on the cross sectional topology of the anode. Furthermore, as discussed in section 3.1, the concentration variations of reactants are predictable by neglecting the convection and only considering the diffusion. Thus, the gradient of ϕ can be obtained by solving the Laplace equation for a given anode design. Figure 7(b) shows the distribution of ϕ in the cross-sectional area of the cell for reference case.

The amount of local forced convective heat transfer q_{ht} (W/m^2) is calculated using the heat transfer coefficient h,

$$q_{ht} = h(T_{sol} - T_{gas}). \qquad (17)$$

In order to determine the heat transfer coefficient, the Nusselt numbers for the parallel plates (Nu_H = 8.235) and the square duct (Nu_H = 3.599) (Shah and London, 1978) are used for the air and fuel channels, respectively.

Figure 8 illustrates the distributions of T_{ele} and i_{ele}, and V_{cell} predicted by this model. These distributions show good agreement with full three-dimensional simulation. Furthermore, these results can be obtained with computational time 1/10^5 that of three-dimensional simulation. Due to this low computational cost, the present cell model can be used for the performance analysis of the cell in a large-scale model, such as a cell stack or whole power generating system. In the next section, the effect of design parameters on the cell performance is discussed by using this model.

4.2 COMPUTATIONAL RESULTS AND DISCUSSIONS

Effect of anode microstructure

Figure 9 shows the output voltage for different pore diameters of the porous anode $d_{p,an}$. A remarkable voltage drop is observed when $d_{p,an}$ is small. The difference of $d_{p,an}$ does not influence the heat transfer in the cell. Namely, the output voltage is determined exclusively by characteristics of mass transfer.

Figure 10 illustrates the normalized molar fraction of H_2 in the y-z plane with different $d_{p,an}$ obtained by three-dimensional simulation. The shortage of H_2 on the TPB becomes significant in the case of d_p = 0.75 μm. As mentioned in section 3.1, the

Copyright © 2006 by ASME

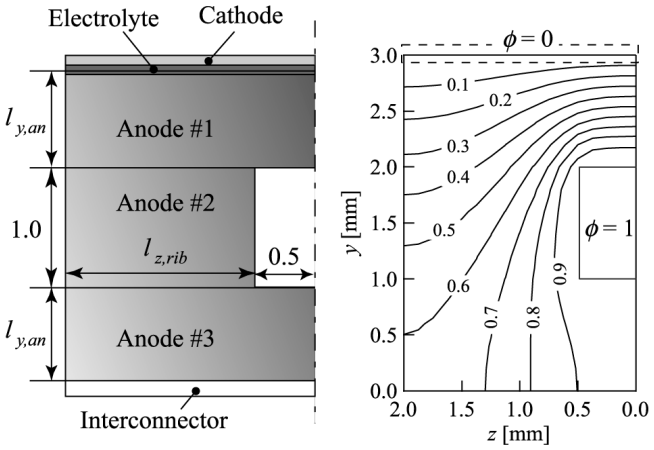

(a) Segmented structure (b)Distribution of ϕ (Ref. case).

Fig. 7 Cross section of the one-dimensional plug flow model.

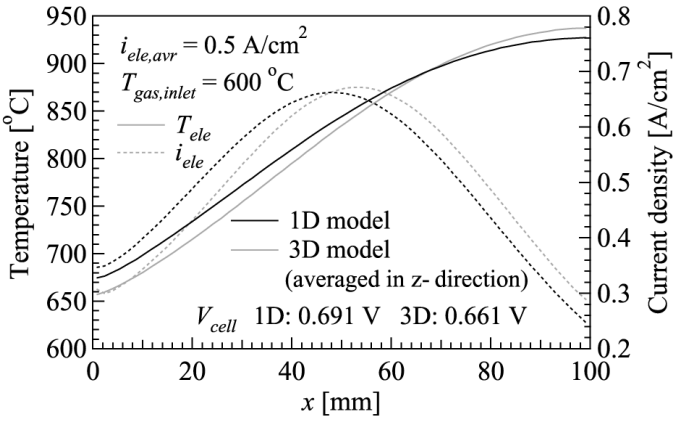

Fig. 8 Distributions of electrolyte temperature and current density (Reference case).

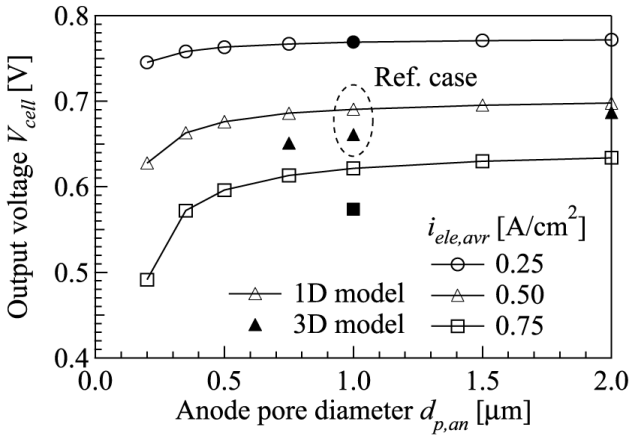

Fig. 9 Output voltage for different pore diameter of porous anode $d_{p,an}$.

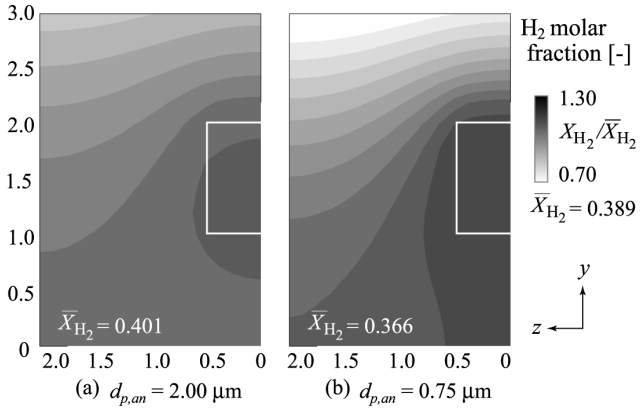

Fig. 10 Distribution of H_2 molar fraction on the *y*-*z* at x = 50.

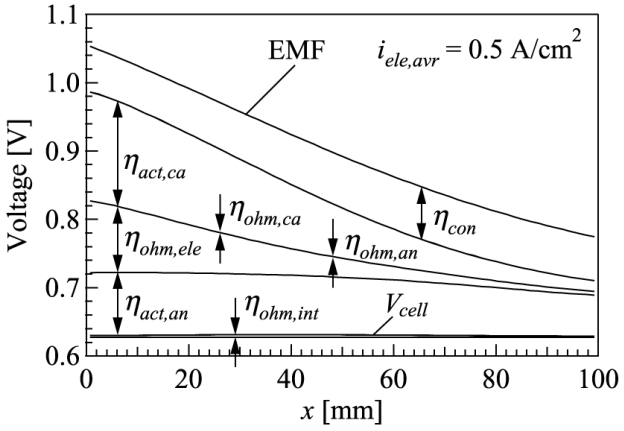

Fig. 11 Distributions of EMF and overpotentials with $d_{p,am}$ = 0.2 μm.

mass transfer in the cell is dominated by diffusion. As suggested by Eq. (6), the effective diffusivity is determined by the molecular and Knudsen diffusivities. When $d_{p,an}$ is large, the magnitude of Knudsen diffusivity is almost the same as that of the molecular diffusivity. In this case, the effective diffusivity slightly increases over that in the reference case. In counterpart, with the decrease of $d_{p,an}$, the effective diffusivity is drastically reduced. Since the Knudsen diffusivity is proportional to $d_{p,an}$, its value becomes smaller than the molecular diffusivity, and it results in poor diffusion of H_2 and H_2O in the anode. As shown in Fig. 11, this poor diffusion leads to the increase of both concentration overpotential (η_{con}) and anodic activation overpotential ($\eta_{act,an}$). This tendency is remarkable for higher average current densities due to the increase of the local reaction amount. Thus, the anode with large material grains is recommended for enhancement of the mass transfer in the cell. In the present study, parameters α and γ for the activation overpotential are set constant regardless of $d_{p,an}$. However, Chan and Xia (2001) showed that the activation overpotential is reduced when fine grains are used as the anode material, because of the increased TPB area. They also pointed out that influence

Copyright © 2006 by ASME

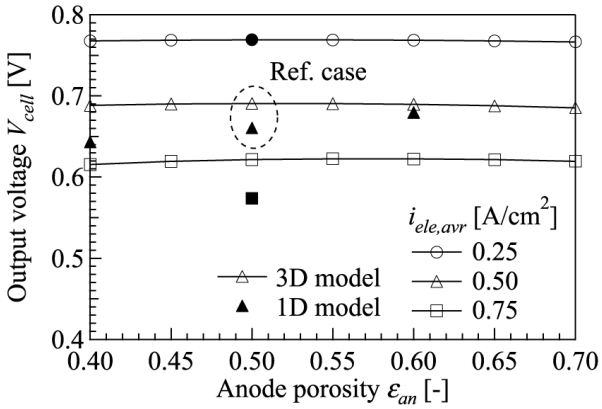

Fig. 12 Dependence of output voltage on anode porosity.

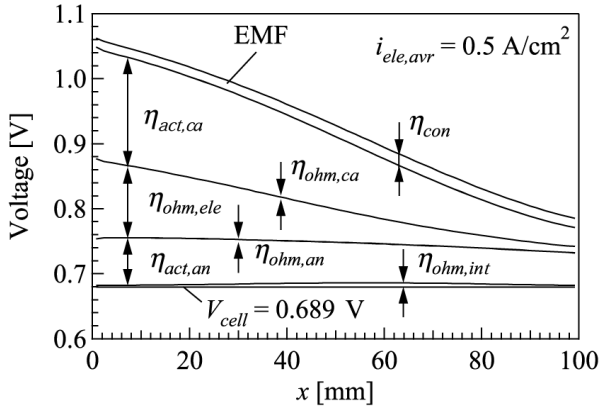

Fig. 13 Dependence of EMF and overpotentials with anode porosity ε_{an} = 0.6.

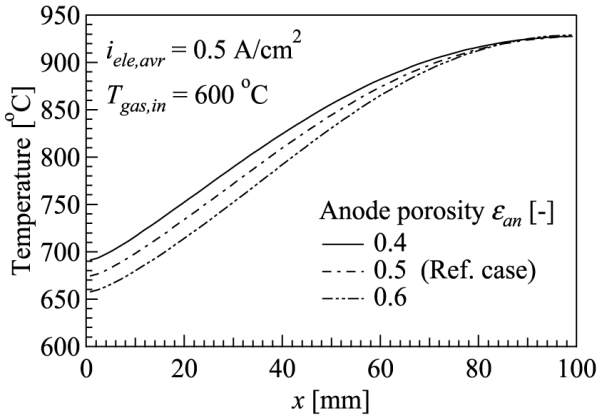

Fig. 14 Distributions of electrolyte temperature on anode porosity.

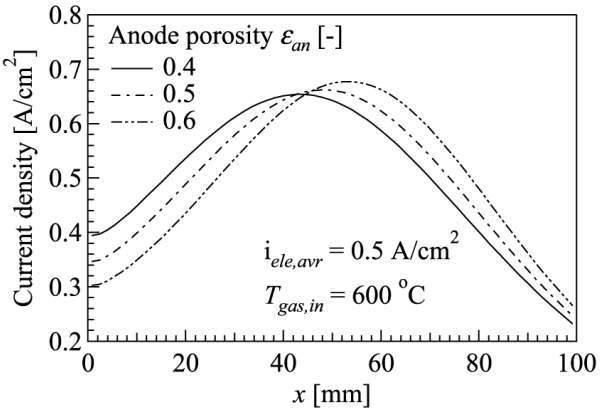

Fig. 15 Dependence of electrolyte current density on anode porosity.

of the anode thickness on the cell performance is considerably small. This knowledge, combined with the present results, implies that a better performance may be achieved using a material with large particles for the gas diffusion layer, and fine particles for the thin reaction layer. The cell with this design concept is made by Kim et al. (2005), and, in fact, showed illustrious performance.

As shown in Fig. 12, the output voltage is less sensitive to the anode porosity ε_{an} than $d_{p,an}$. As Eq. (6) suggests, the effective diffusivity becomes larger when ε_{an} is large. As the effective diffusivity is increased, the shortage of H_2 and the stagnation of H_2O are improved. Consequently, as shown in Fig. 13, the concentration overpotential (η_{con}) is reduced.

On the other hand, the effective thermal conductivity of porous media $\lambda_{eff} = \varepsilon\lambda_{gas} + (1-\varepsilon)\lambda_{sol}$ becomes smaller with increasing ε_{an}. As shown in Fig. 14(a), the solid temperature becomes lower at the cell inlet with the decrease of λ_{eff}. This leads to increases in the activation overpotential η_{act} and the ohmic loss of the electrolyte ($\eta_{ohm,ele}$), and the local current density becomes smaller as shown in Fig. 15. As a whole, a trade-off occurs between the mass transfer enhancement and heat transfer degradation when ε_{an} is varied. Thus, V_{cell} is almost constant regardless of ε_{an}. The computational result also indicates that this trade-off is optimized when ε_{an} = 0.6.

Effect of anode cross-sectional configuration

Figures 16 shows V_{cell} and the volumetric power density W_{cell} of the cell for different anode thickness $l_{y,an}$ and rib width $l_{z,rib}$. Here, W_{cell} is defined as

$$W_{cell} = \frac{V_{cell} \cdot i_{ele,avr}}{l_{y,cell}} , \qquad (18)$$

where $l_{y,cell}$ is the cell thickness, which is the summation of electrolyte, electrodes and interconnector thicknesses. The values of $l_{y,an}$ and $l_{z,rib}$ are changed with increment of 0.2 and 0.25 mm, respectively.

In the case of $i_{ele,avr}$ = 0.5 A/cm^2, V_{cell} is maximized when $l_{y,an}$ = 1.6 mm and $l_{z,rib}$ = 0.5 mm. However, the gain of V_{cell} over the reference case is small, and W_{cell} drops considerably. In contrast, W_{cell} increases proportionally to $l_{z,rib}$. When $l_{y,an}$ = 0.2

Copyright © 2006 by ASME

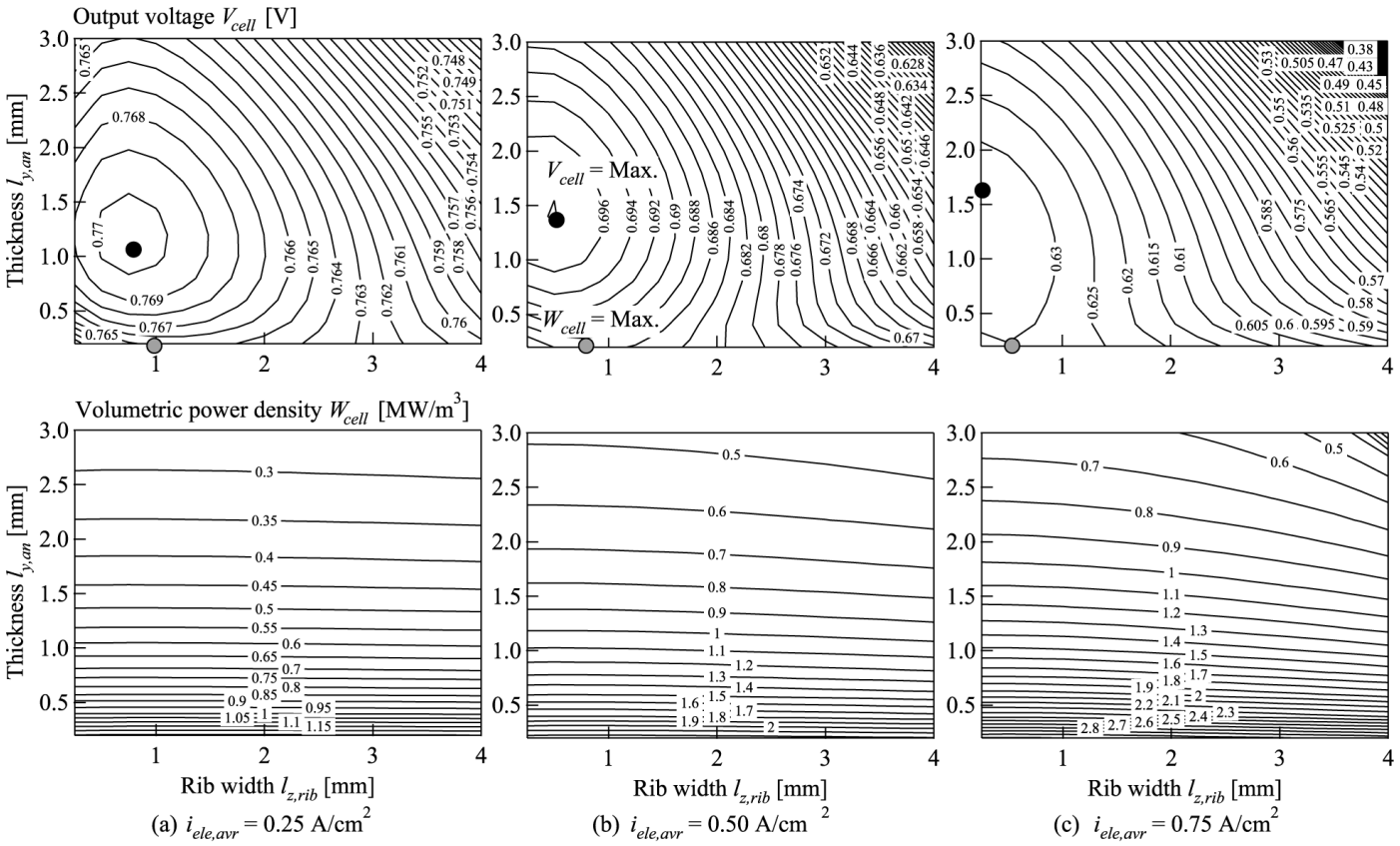

Black dot: Max. V_{cell} case. Gray dot: Max. W_{cell} case

Fig. 16 Output voltage V_{cell} and volumetric power density W_{cell} for different anode configurations.

mm, W_{cell} is drastically increased with $l_{z,rib}$ = 0.5 mm compared with reference case, whereas the drop of V_{cell} is negligibly small. The values of $l_{y,an}$ and $l_{z,rib}$ that maximize V_{cell} or W_{cell} are almost constant regardless of $i_{ele,avr}$.

When the cell has a thick or wide rib anode, the diffusion length of reactants in the porous anode becomes longer. This leads to severe fuel shortage on the TPB and increased concentration overpotential. In contrast, the inlet temperature of the cell is kept high by the enhanced heat conduction. This improved temperature distribution can reduce both activation overpotential and ohmic loss of the electrolyte. Thus, the effect of improved heat transfer compensates the deterioration of mass transfer, and this fact makes V_{cell} insensitive to the anode configuration. This insensitivity suggests that the variation of W_{cell} is not caused by the change of V_{cell} but by the difference of $l_{y,an}$. Namely, a thinner anode is advantageous to achieve high W_{cell}. The optimal $l_{z,rib}$ is 0.75 to obtain high V_{cell} for broad range of $i_{ele,avr}$.

5. CONCLUSIONS

Numerical simulation and modeling of the heat/mass transfer and electrochemical reaction in the anode-supported flat-tube solid oxide fuel cell (FT-SOFC) has been carried out. Through the present parametric survey, the following conclusions are obtained.

1. The transport and reaction phenomena vary mainly in the streamwise direction. Exceptionally, H_2 and H_2O show large concentration gradients in the cross section due to insufficient diffusion in the porous anode. Based on these results obtained by detailed simulation, a simple one-dimensional plug-flow model of the cell is developed. This model can precisely predict the cell performance at much less computational cost.

2. For fixed TPB length, the output voltage of the cell is seriously degraded when the porous anode has small pore diameter. With decreasing the pore diameter, the mass transfer in the cell is considerably degraded by deterioration of the Knudsen diffusion. Further detail investigation considering the change of TPB is required to determine the optimal pore diameter of the anode material. In contrast, the output voltage of the cell is insensitive to the anode porosity due to a trade-off between the effect of heat transfer and that of mass transfer.

Copyright © 2006 by ASME

3. The output voltage is also insensitive to the anode thickness and the rib width. When the cell has a thin anode with a narrow rib, drastic increase of volumetric power density can be achieved with small voltage drop.

ACKNOWLEDGEMENTS

We would like to thank Professor Yuji Suzuki at the University of Tokyo for beneficial discussion and advice. This research was supported through The 21st Century COE Program, "Mechanical Systems Innovation", by the Ministry of Education, Culture, Sports, Science and Technology of Japan (MEXT).

NOMENCLATURE

C_p	Isobaric specific heat (J/kgK)
D_i	Diffusivity of the reactant *i* (m^2/s)
d_p	Pore diameter of the porous media (m)
E	Electromotive force (EMF) (V)
F	Faraday constant : 9.649×10^4 (C/mol)
ΔG^o	Standard Gibbs' free-energy change of the reaction (J/mol)
i	Current density (A/m^2)
M_i	Molar weight of the reactant *i* (kg/mol)
P	Pressure (Pa)
p_i	Partial pressure of the reactant *i* (Pa)
Q	Heat generation (W/m^3)
R	Gas constant : 8.314 (J/mol K)
T	Temperature (K)
u, *u*, *v*, *w*	Flow velocity (m/s)
V_{cell}	Output voltage of the cell (V)
W_{cell}	Volumetric power density of the cell (W/m^3)
x, *y*, *z*	Cartesian coordinates (-)
X_i	Molar fraction of the reactant *i* (-)
Y_i	Mass fraction of the reactant *i* (-)

Greeks

ε	Porosity of the porous media (-)
η_{act}	Activation overpotential (V)
η_{con}	Concentration overpotential (V)
η_{ohm}	Ohmic loss (V)
κ	Flow permeability in the porous media (m^2)
λ	Thermal conductivity (W/mK)
μ	Viscosity (Pa s)
ρ	Density (kg/m^3)
σ	Resisivity (Ω cm)
τ	Tortuosity of the porous media (-)

Subscripts and superscript

an	Anode
avr	Average
ca	Cathode
ele	Electrolyte
gas	Gas
H_2	Hydrogen
H_2O	Water vapor
int	Interconnector
O_2	Oxygen
sol	Solid
–	averaged value in the cross section

REFERENCES

Aguiar P., Adjiman, C. S. and Brandon, N. P., 2004, "Anode-supported intermediate temperature direct internal reforming solid oxide fuel cell. I: model-based steady-state performance," J. Power Sources, **138**, pp. 120-136.

Asaeda, M., Nakano, M. and Toei, R., 1974, "Isobaric diffusion of gases in packed beds of fine particles," J. Chem. Eng., Jpn., **7**(3), pp. 173-180.

Bird, R. B., Stewart, W. E. and Lightfoot, E. N., 2002, Transport Phenomena 2nd Ed., Wiley, New York.

Campanari, S. and Iora, P., 2004, "Definition and sensitivity analysis of a finite volume SOFC model for a tubular cell geometry," J. Power Sources, **132**, pp. 113-126.

Carniglia, S. C., 1986, "Construction of the tortuosity factor from porosimetry," J. Catal., **102**, 401-418.

Chan, S. H., Khor, K. A. and Xia, Z. T., 2001, "A complete polarization model of a solid oxide fuel cell and its sensitivity to the change of cell component thickness," J. Power Sources, **93**, pp. 130-140.

Chan, S. H. and Xia, Z. T., 2001, "Anode micro model of solid oxide fuel cell," J. Elcetorchem. Soc., **148**(4), pp. A388-A394.

Costamagna, P. and Honegger, K., 1998, "Modeling of solid oxide heat excahnger integrated stacks and simulation at high fuel utilization," J. Electrochem. Soc., **145**(11), pp. 3995-4007.

Furguson, J. R., Fiard, J. M. and Herbin, R., 1996, "Three-dimensional numerical simulation for various geometries of solid oxide fuel cells," J. Power Sources, **58**. pp. 109-122.

Giuseppe, G., 2005, "High power density cell development at Siemens Westinghouse," Proc. Solid Oxide Fuel Cells IX, 322-332.

Kim, S. D., Hyun, S. H., Moon, J., Kim, J-H. and Song, R. K., 2005, "Fabrication and characteristics of anode-supported electrolyte thin films for intermediate temperature solid oxide fuel cells," J. Power Sources, **139**, pp. 67-72.

Li, P. W. and Chyu, M. K., 2005, "Electrochemical and transport phenomena in solid oxide fuel cells," J. Heat Transfer, **124**, pp. 219-229.

Majda, A. and Sethian, J., 1985, "The derivation and numerical solution of the equations for zero Mach number combustion," Combustion Sci. Tech., **42**, pp. 185-205.

Shah, R. K. and London, A. L., 1978, Laminar flow forced convection in ducts (Supplement 1 of Advances in heat transfer edited by Irvine, T. F. Jr. and Hartnett, J. P.), Academic press, New York.

Yakabe, H., Ogiwara, T., Hisinuma, M. and Yasuda, I., 2001, "3-D model calculation for planar SOFC," J. Power Sources, **102**, pp. 144-154.

Copyright © 2006 by ASME